Self-Powered Single Multifunctional Tactile Sensor for Simultaneous Detection of Dynamic and Static Pressure and Temperature Inspired by Skin Sensory Functions

Ey-In Lee, Hee-Jin Ko, Jongbaeg Kim, Jin-Woo Park*

Ey-In Lee, Jin-Woo Park

Department of Materials Science and Engineering, Yonsei University, Seoul 03722, Republic of Korea
E-mail: jwpark09@yonsei.ac.kr

Hee-Jin Ko, Jongbaeg Kim

Department of Mechanical Engineering, Yonsei University, Seoul 03722, Republic of Korea

Abstract

In electronic skin technology, achieving broad sensing capabilities with minimal sensors is essential for developing energy-efficient and compact systems. In this study, the triboelectric mechanism is employed for self-powered operation, and an ionogel is integrated with a triboelectric pressure sensor in a parallel configuration, generating characteristic voltage profiles that encode information about dynamic pressure, static pressure and temperature. This configuration enables the simultaneous detection of three stimuli with a single sensor, contributing to a compact system. The profiles result from interactions between ions and triboelectric charges, which are driven by changes in the impedance and interfacial capacitance within the ionogel under applied stimuli. By analyzing the voltage profiles based on a physical understanding of the triboelectric and ionic components, the sensing mechanism is validated through correlation of parameter variations with component properties under different stimuli. The analyzed parameters effectively quantify the three applied stimuli, ensuring accurate discrimination. Beyond real-time discrimination of pressure and temperature, the ability to separate pressure into dynamic and static components enables the sensor to evaluate the degree

1

of softness of objects and detect damage points under stimuli. This multifunctional tactile sensor has significant potential for advancing electronic skin technologies, with promising applications in smart prosthetics, adaptive robotics, and extended reality (XR) technologies.

Keywords: bimodal tactile sensors, self-powered sensors, triboelectricity, ionics

1. Introduction

Human skin, which serves as a physical barrier between the body and the external environment, provides tactile information to the central nervous system [1]. Sensory receptors, including mechanoreceptors, thermoreceptors, and nociceptors located within the epidermis or dermis [2-3], detect external stimuli and relay signals to sensory neurons [4]. These activated sensory neurons then transmit the encoded signal to the brain or spinal cord, enabling sensory perception [5]. In the initial phase of sensory perception, skin discriminates various external stimuli through distinct receptors. Electronic skin (e-skin), which has been developed to emulate the sensory functions of human skin, must possess multisensory capabilities while maintaining low energy consumption [6]. This requirement is crucial for enhancing its applicability in diverse fields, such as humanoid robotics, biomimetic prosthetics, and artificial intelligence [7-10].

Considering the sensory functions of human skin, e-skin must detect elements such as pressure, strain, humidity, and temperature [11-12]. Human skin senses strain through slow-adapting mechanoreceptors and humidity by integrating signals from both mechanoreceptors and thermoreceptors [13]. Since mechanoreceptors primarily detect pressure and thermoreceptors detect temperature, sensing both pressure and temperature is fundamental for broader sensory detection [2,13]. Given the importance of multisensory, particularly pressure and temperature, sensing, extensive research has focused on combining various sensing mechanisms and effectively decoupling signals [14-15]. The conventional strategy involves developing sensors that measure a single target stimulus and integrating them into one platform [16-18]. Since such an integrated system utilizes several distinct sensors, it is beneficial for extracting and interpreting the individual outputs corresponding to the input stimuli. However, this approach often necessitates complex sensor structures and manufacturing processes [15,19]. Additionally, the individual data processors and transmitters required for each sensor lead to a bulky system, posing a significant challenge for future e-skin technologies, which demand simplicity for seamless integration in diverse applications [11,15].

2

An alternative approach is to utilize a single sensor that responds to multiple stimuli. This design, with a simple discrimination method, includes a sensor that exhibits different types of output signals (voltage, current, resistance, capacitance, etc.) depending on the type of input stimulus [20-25]. For example, combinations of pyroelectric and piezoresistive mechanisms [20], thermoelectric and piezoresistive mechanisms [21-24], and thermoresistive and piezophotonic mechanisms [25] have been employed in temperature–pressure dual-sensing sensors. These sensors can be used to discriminate between multiple target stimuli by analyzing the temperature–pressure-dependent behavior. However, such designs cannot simultaneously sense multiple stimuli, as they require connection to different measuring apparatuses depending on the specific target stimulus.

To achieve a simultaneous multisensory capability, the development of a single sensor that produces a single type of output signal for multiple stimuli, along with an appropriate decoupling strategy, is essential. Several studies have proposed sensors capable of simultaneously detecting temperature and pressure [15,26-28], in which the pyroelectric mechanism is typically utilized for temperature sensing, which is decoupled from pressure sensing through the differing response times of piezoelectric and triboelectric mechanisms. However, since these mechanisms produce signals only at the moment of stimulus application, they face challenges in sensing sustained mechanical or thermal stimuli. Similar to human skin, e-skin should be able to analyze its surroundings by detecting not only dynamic pressure but also static pressure [29-30]. Static pressure perception is activated when objects are held with a constant force, whereas dynamic pressure perception is activated upon contact with the surface of an object, such as during throwing, catching, or slipping, during which the applied pressure rapidly changes [31-35]. To our knowledge, no research has yet addressed the simultaneous detection of dynamic pressure, static pressure, and temperature. To detect and differentiate these three types of stimuli with a single sensor using a simplified decoupling strategy, a potential solution is to design structures with sensing components that each respond to a specific stimulus while generating the same type of output signal.

In addition to a multisensory capability, e-skin technology must exhibit various other essential features, including mechanical flexibility, biocompatibility, transparency, and a self-healing ability [36-39]. Self-powering is also an increasingly critical property, as it enables the system to operate with reduced power consumption. In terms of pressure detection, four sensing mechanisms are utilized in artificial sensors: piezoresistive, capacitive, piezoelectric, and triboelectric mechanisms [40-41]. Given that piezoelectric and triboelectric sensors generate

3

charges under mechanical stimuli, they are suitable for self-powering systems, unlike piezoresistive and capacitive sensors.

From the perspective of materials, electrically conducting materials are typically used for piezoresistive, thermoresistive, and thermoelectric sensors, whereas dielectric materials are commonly employed in capacitive, piezoelectric, triboelectric and pyroelectric sensors [42-45]. Given that ionic materials exhibit both electrical conductivity and capacitive properties, they provide a distinct advantage for iontronic sensors, enabling their application under various sensing mechanisms [46]. Furthermore, the combination of resistive and capacitive features allows diverse signal profiles when interacting with piezoelectric or triboelectric charge generators [47-48]. Ionic migration along an electric field elongates the peak-like voltage generated by piezoelectric charge generators, enabling the detection of both dynamic and static pressures with a single sensor [48]. In addition to assisting in static pressure detection, ionic materials also possess capacitive properties under a temperature difference [46]. Ionic materials can be formed into solid-state gels to ensure mechanical stability, portability, and broad applicability. Ionogels, formed by swelling polymer networks in ionic liquids, can be utilized to mitigate the water evaporation issues associated with hydrogels while maintaining a sufficient ionic conductivity [49-50]. Ionogels, which have been extensively utilized in iontronic sensors, are ideal for e-skin technology with a multimodal capability.

In this study, a self-powered tactile sensor that simultaneously detects pressure and temperature via ionic and triboelectric mechanisms is demonstrated. The sensor comprises a triboelectric component and an ionic component, both of which produce identical types of output signals. The triboelectric component, with its dome-shaped structure, can detect dynamic pressure and functions as a charge supplier for static pressure sensing in the self-powered system. The ionic component, which modulates the voltage signal based on the impedance and triboelectric-supplied charges, is responsible for static pressure detection. Additionally, the capacitive property of the ionic component enables discrimination of the temperature difference. Furthermore, the two separate components are electrically connected in parallel to minimize interference between them and preserve their individual functionalities. Since each component is dedicated to sensing a specific stimulus, the sensor can analyze overlapping output signals through a simple decoupling strategy, despite both components producing identical types of output signals. Additionally, based on a physical and electrical understanding of the sensing behavior, the output voltage can be quantitatively defined by analytical formulas, which can clearly explain the sensing mechanisms.

4

2. Results and Discussion

2.1. Concept and functions of the parallel-connected triboelectric generator and ionogel tactile sensor (p-TITS)

A combination of triboelectric and ionic features is utilized for the simultaneous detection of dynamic pressure, static pressure and temperature with a single sensing unit in this study. For triboelectric charges and ions to efficiently interact electrically, they should form a parallel-connected triboelectric generator and ionogel tactile sensor (p-TITS) (Fig. S1a). As shown at the bottom right of Fig. 1a, the triboelectric component of the p-TITS generates charges in contact-separation mode via the interaction of aluminum (Al) foil with dome-structured polydimethylsiloxane (PDMS). These generated charges influence the ions in the ionic component through the shared common indium tin oxide-coated polyethylene terephthalate (PET/ITO) electrodes. As shown in Fig. S1a, the ionic component is located on the lateral sides of the triboelectric component, with two common current collectors aligned vertically.

The voltage profile obtained upon stimulus application is shown at the top right of Fig. 1a. When a touch occurs, a peak-like voltage is generated by the triboelectric generator, perceiving the touch as a dynamic pressure. The voltage then decays according to the electrical properties (resistance and capacitance) that depend on temperature. When the pressing is sustained, the voltage remains at a level higher than the baseline that corresponds to the magnitude of the static pressure. In summary, the dynamic pressure is detected at the onset of the stimulus, the temperature is indicated during the decay period, and the static pressure is sensed when the voltage profile stabilizes. Since the voltage profile contains three types of information (dynamic pressure, static pressure, and temperature) at different times, the pressure and temperature can be discriminated from a single voltage profile.

Fig. 1b shows the variations in the voltage profiles under two stimuli of different magnitudes. The peak-like voltage observed at the moment of stimulus application originates from the triboelectric mechanism, with a higher pressure resulting in a higher voltage output. With increasing pressure, the overall voltage increases while maintaining a consistent profile. In contrast, thermal stimuli induce changes in the voltage profile shape, with a steeper decay slope observed at lower temperatures, as the electrical properties of the ionogel vary with temperature. Under simultaneous changes in pressure and temperature, analysis of the voltage profile, especially in terms of the peak voltage and decay slope, enables discrimination of both the magnitude and type of applied stimuli.

5

Moreover, by detecting both dynamic and static pressures, the p-TITS can be used to evaluate the degree of softness of a touched object. Typically, strain sensors and pressure sensors are integrated to emulate human skin in sensing softness by combining the degrees of skin stretching and compression [51-52]. The surface deformation of a target object under a given pressure can be measured using such a combined system. However, instead of detecting both strain and pressure, dynamic and static pressure sensing can be used to evaluate the softness of an object [30]. As the sensed material becomes harder, the signal obtained under a dynamic pressure increases, whereas the signal observed under a static pressure is lower (Fig. 1c). Both types of pressures also yield different values depending on the level of applied pressure. However, they exhibit the same variation trends with increasing pressure but opposite trends based on the softness of the object, allowing the cause of the voltage variation to be distinguished. To ensure reliable detection of the softness of an object, both dynamic and static pressures must be detected. Unlike previous systems that utilize two sensors to measure the softness of an object, the p-TITS achieves softness detection with a single sensor by evaluating both dynamic and static pressures (Fig. 1c).
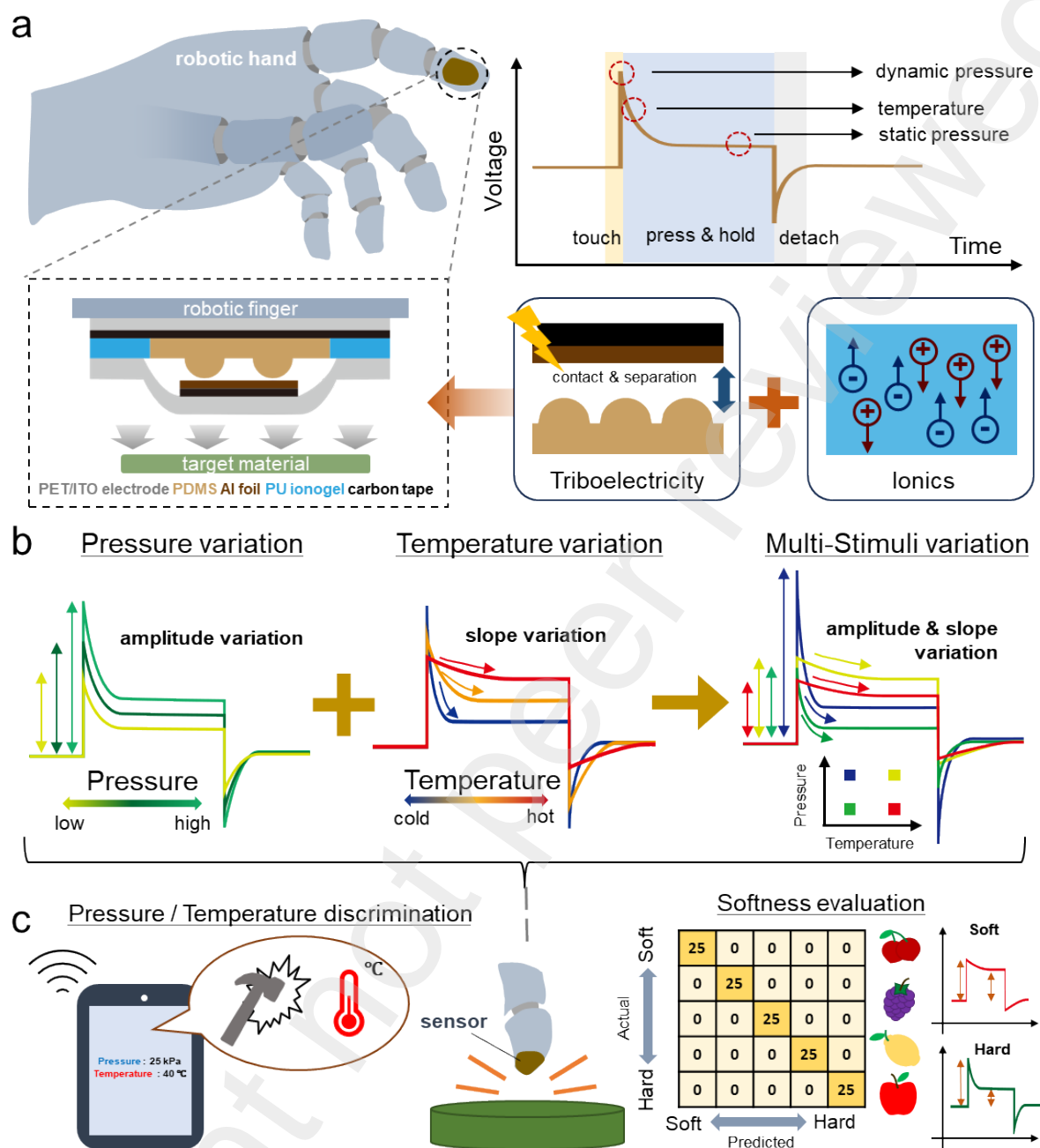
6

Figure 1. a) Schematic representation of the components of the p-TITS attached to a robotic finger and its voltage profile in response to external stimuli. b) Voltage profiles under various pressures and temperatures. c) Softness perception and pressure/temperature discrimination capabilities of the p-TITS demonstrated through its application on a robotic finger.

2.2. Design and properties of the p-TITS

Dome-shaped structured PDMS was utilized to fabricate a triboelectric pressure sensor based on variations in the contact area between the PDMS and Al foil upon pressure application [53]. A negative hemisphere-patterned mold was 3D printed to create structured

7

PDMS, which formed dome-shaped structures with a radius of 500 μm without any residual PDMS remaining in the mold (Fig. 2a). Top and side views of the dome-shaped PDMS are shown in Fig. S1b. Owing to the lower impedance of the ionic component than of the parallel-connected triboelectric component, the electrical properties of the integrated p-TITS are predominantly governed by the ionic component. The electrical behavior is influenced by two resistive factors (contact resistance and ionic resistance) and two capacitive factors (interfacial capacitance and polymer matrix capacitance) [54]. Integrated sensors with various [EMIM][BF$_4$] concentrations (1, 2, and 4 wt%) in polyurethane (PU) ionogels exhibit similar shapes of the Nyquist plots obtained via electrochemical impedance spectroscopy (EIS), each of which is characterized by a single semicircle, with a higher concentration of [EMIM][BF$_4$] resulting in a reduced resistance, as evidenced by the smaller semicircle radius in the Nyquist plots (Fig. 2b). Furthermore, the voltage response under pressure also exhibits a characteristic profile, starting with a peak-like voltage followed by a decay process and a stable voltage higher than the baseline (Fig. S2a). This characteristic voltage profile arises from the combined effects of the triboelectric charge generator and the ionogel. The consistent electrical characteristics and voltage profiles observed for sensors with various ionic concentrations validate the stability of the fabrication method and confirm the reliability of the sensor properties, thus verifying the concept of the p-TITS (Fig. 2b,S2a).

Cyclic voltammetry (CV) data were obtained at increasing voltage scan rates ranging from 5 mV/s to 100 mV/s to verify the electrical stability and quantify the interfacial capacitance of the p-TITS. Within the applied potential range of -0.5 V to 0.5 V, the ionic component remains stable, forming an electric double layer without redox reactions (Fig. 2c). The square-like shape of the CV curve at lower scan rates indicates an interfacial capacitance of 3.95 μF. Since the triboelectric component generates voltages below 0.5 V, the p-TITS maintains its ionic properties through electric double layer formation.

As a pressure sensor, the p-TITS exhibits higher voltages under increased pressure, with sensitivities of 0.03419 mV/kPa for dynamic pressure and 0.00627 mV/kPa for static pressure. Although the pressure sensitivity is relatively low, the sensor demonstrates a high degree of linearity (Fig. 2d,e). A force of 3 N was applied at pressure frequencies ranging from 0.05 Hz to 5 Hz to evaluate the ability of the p-TITS to detect various types of pressures, resulting in consistent voltage outputs (Fig. 2f). The voltage profiles were recorded at a sampling rate of 1000 samples per second to capture all the signals generated at rapid rates. During postprocessing, a 50 Hz low-pass filter was applied to eliminate the 60 Hz noise

8

originating from the power supply of the measuring apparatus (Fig. S3a). Additionally, fast Fourier transform (FFT) analysis of the raw voltage data validates the voltage profiles generated by the p-TITS (Fig. S3b). For both low-frequency pressures (below 0.05 Hz) and high-frequency pressures (above 1 Hz), the FFT data reveal prominent peaks at 60 Hz and 120 Hz, corresponding to noise from the power supply. However, unlike the FFT data for low-frequency pressures, the high-frequency pressure data exhibit additional peaks at 1.6 Hz and its multiples, confirming that the voltage profile originates from the p-TITS under pressure application.

The simultaneous sensing of dynamic pressure, static pressure, and temperature is illustrated in Fig. 2g-i. Fig. 2g shows the voltage output with increasing pressures of 10, 30, 50, 70, and 90 kPa. A similar trend is observed for static pressures in Fig. 2h. The experimental setup for applying both types of stimuli is shown in Fig. S4a. The p-TITS was attached to a pushing machine and pressed against a stationary part consisting of a Peltier module, a heat sink, and Al foil. The Peltier module was controlled by a DC voltage supply, with the heat sink preventing excessive heating of the system. The Al foil was affixed to the top of the Peltier module to eliminate potential electrical interference. Under constant temperatures of 25 °C, 35 °C, and 45 °C, a pressure of 50 kPa was applied, simulating touch interactions accompanied by both mechanical and thermal stimuli. As the applied temperature increases, the overall voltage profile and the rate of voltage decay decrease (Fig. 2i). Compared with Fig. 2g, which shows consistent voltage decay profiles under constant temperature conditions, distinct differences in the decay profiles are observed at various temperatures. Furthermore, thermogravimetric analysis (TGA) data confirm the thermal stability of the PU ionogels, which retain 99.5% of their mass up to 160 °C (Fig. S4b).
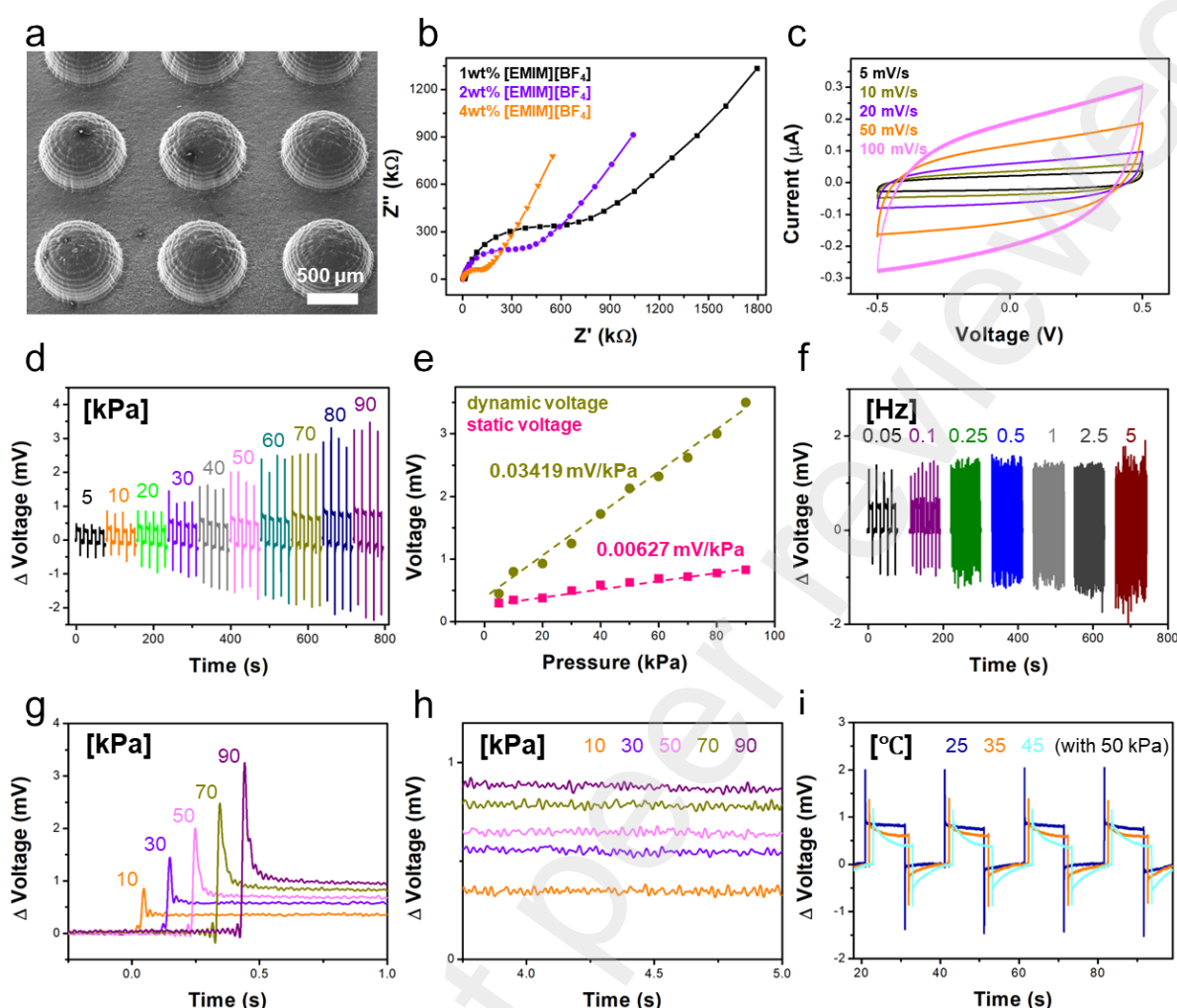
9

Figure 2. a) SEM images of the dome-shaped triboelectric component. b, c) EIS and CV data of the p-TITS with different ionic concentrations. d) Voltage profiles under various pressures. e) Pressure sensitivity analysis. f) Voltage profiles of the p-TITS at different pressure frequencies. g and h) Dynamic and static voltage profiles under pressure, respectively. i) Voltage profiles at different temperatures under a pressure of 50 kPa.

2.3. Sensing mechanism of the p-TITS

To verify the sensing mechanism of the p-TITS, the PU ionogel of the p-TITS was replaced with a PU film to fabricate the triboelectric component. The triboelectric pressure sensing properties are illustrated in Fig. 3a, which shows a peak-like voltage response without the ability to sense static pressure. Considering the effect of temperature on the triboelectric performance, the output voltage can be influenced by temperature-induced changes in the ability of the contact layer to store and transfer electrons [55]. As shown in Fig. 3b, the triboelectric component generates lower voltages as the temperature increases.

10

This trend is further illustrated in Fig. 3c, where an increase in pressure leads to a higher voltage output, whereas an increase in temperature results in a decreased voltage output. The decreased voltage output at higher temperatures, as observed in Fig. 2i, is thus attributed to the reduced triboelectric performance.

The electrical properties of the ionic component were investigated under various pressure and temperature conditions. The ionic component, with an area of 1 cm × 1 cm, was separately fabricated without the triboelectric component. For the fabricated ionic component, carbon tape was utilized between one PET/ITO electrode and the PU ionogel for attachment. For the other PET/ITO electrode, the PU ionogel was directly cast so that no additional adhesive was needed. Pressures of 20, 50, and 80 kPa were applied, along with temperatures of 25 °C, 35 °C, and 45 °C. CV was conducted to calculate the interfacial capacitance formed by the electric double layer. The area of the CV curve in Fig. 3d, indicating the interfacial capacitance, remains constant under different pressure conditions but increases with increasing temperature. In the case of EIS, similar profiles are observed at the same temperature regardless of the applied pressure, similar to the CV data. The radius of the semicircle in the Nyquist plot, which corresponds to the resistance term, decreases as the temperature increases (Fig. 3e). The resistance is influenced primarily by temperature, whereas it remains relatively unchanged under varying pressure. This trend is also evident in the Bode plot, which shows the impedance differences at low-frequency voltages under different temperature conditions (Fig. 3f).

The Bode plot of the ionic component indicates an equivalent circuit composed of two resistors and two capacitors. The two resistors are dominant in the voltage frequency ranges above 100 kHz and between 10 Hz and 100 Hz, whereas the two capacitors are dominant in the ranges below 10 Hz and between 100 Hz and 100 kHz. In Fig. S5a, the Bode plot of the ionic component is compared with that of a sample without carbon tape between the PU ionogel and one of the PET/ITO electrodes. The Bode plot shows that the sample without carbon tape consists of one resistor and one capacitor. The resistor term at high voltage frequencies corresponds to the ionic resistance, and the capacitor term under low voltage frequencies corresponds to the interfacial capacitance. As the ionic component and the compared sample share a common PU ionogel, the resistor term at high frequencies for the ionic component with carbon tape (Fig. 3f) represents the ionic resistance. The second resistor term, showing a high resistance of over 10 kΩ, represents the contact resistance originating from the carbon tape. The results indicate that an increase in the temperature leads

11

to a decreased contact resistance while a constant ionic resistance is maintained. Conclusively, the electrical properties of the ionic component reveal that the interfacial capacitance increases and the impedance decreases with increasing temperature but remains constant under varying pressure.

The properties of the p-TITS can be categorized based on whether they are influenced by temperature or pressure application, which is closely related to the sensing mechanism. The variations in the interfacial capacitance and impedance with the pressure and temperature conditions calculated for a voltage input of approximately 1 Hz are shown in Fig. 3g. Without any external stimuli, the interfacial capacitance is approximately 9 µF. It increases to 10 µF at 25 °C, 12 µF at 35 °C, and 15 µF at 45 °C with pressure application, indicating a minimal effect from pressure. Additionally, the impedance of approximately 380 Ω decreases to 210 Ω at 25 °C. It further decreases to 100 Ω and 40 Ω at 35 °C and 45 °C while maintaining its value under various pressures. For the triboelectric component, the voltage output decreases with increasing temperature and is also affected by pressure application, as previously discussed regarding Fig. 3c.

Given that the triboelectric component only shows a peak-like voltage when pressure is applied, the subsequent decay profile and stable voltage higher than the baseline can be explained by the ionic component. To verify this, a system without variations in the electrical properties during stimulus application was examined. The triboelectric component and ionic component were externally connected so that the stimulus was applied only to the triboelectric component, as shown on the right side of Fig. 3h. When pressure is applied, a peak voltage representing the dynamic voltage appears in both systems (Fig. 3h). For the voltage generated under static pressure, the p-TITS (with internally connected triboelectric generator and ionogel) exhibits a significantly higher voltage than the externally connected triboelectric generator and ionogel. This voltage difference under static pressure can be explained by the varying properties of the ionic component. Unlike the p-TITS, the externally connected system shows constant ionic properties since pressure is applied only to the triboelectric generator component.

Interestingly, the externally connected system also generates some voltage output under static pressure, unlike the triboelectric component alone. This behavior can be attributed to the ions in the ionic component interacting with the charges generated by the triboelectric component, thereby retaining charges at the interfaces between the electrodes and the PU ionogel. The retention of these charges is shown as a potential difference under static

12

pressure. When a higher pressure is applied to the externally connected triboelectric generator, a higher dynamic voltage is generated, accompanied by a slightly higher static voltage (Fig. S5b). However, since the static voltage generated due to the presence of the ionic component has a significantly lower influence than the variation in the electrical properties of the ionic component, the correlation between the electrical properties and the static voltage should be considered. The reverse trends in the impedance of the ionic component and the voltage can explain the detection of the static pressure [56]. The decrease in the impedance under stimuli shown in Fig. 3g constitutes the main principle underlying the generation of a static voltage. Further correlations can be determined by analyzing the components of the whole voltage profile illustrated in Fig. 4.

As discussed regarding Fig. 2i, the overall voltage profile and the rate of voltage decay decrease as the applied temperature increases. The reduction in the overall voltage profile can be attributed to the diminished triboelectric properties, as shown in Fig. 3c. In terms of the decreased rate of voltage decay, as the electrical properties change at different temperatures regardless of pressure, the ionogel is responsible for the temperature sensing mechanism of the p-TITS. Considering the resistance term of the RC delay as the fixed measurement resistance (10 MΩ) [47], the RC delay increases with increasing interfacial capacitance. An increase in the interfacial capacitance, as shown in Fig. 3g, can be related to a decrease in the voltage decay rate, with an extended voltage profile. As the interfacial capacitance only depends on the temperature, the temperature can be discriminated by measuring the RC constant. Since the electrical properties in Fig. 3g were measured at a sufficient time after stimulus application, the value could be slightly different from the RC constant shown in the voltage profile of Fig. 2i, which was defined by the real-time varying capacitances.
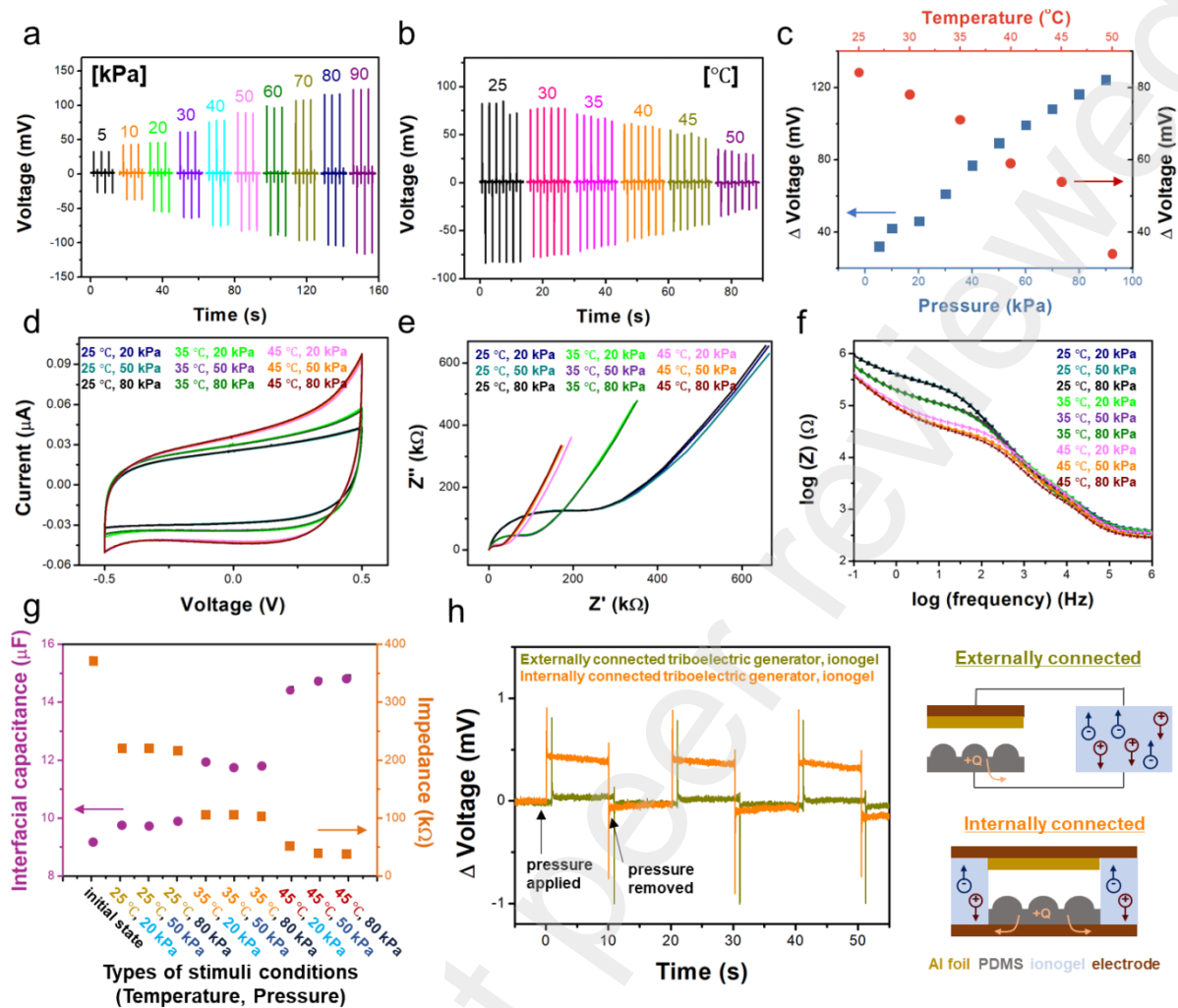
13

Figure 3. a-c) Voltage profiles of the triboelectric component under various pressure and temperature conditions. d) CV curve, e) Nyquist plot, and f) Bode plot of the ionic component under various pressure and temperature conditions. g) Interfacial capacitance and impedance under various pressures and temperatures. h) Comparison of the voltage profiles under pressure in different electrical connection modes.

2.4. Decoupling and reliability

When stimuli (temperature, pressure) are applied, the p-TITS exhibits a characteristic voltage profile consisting of the following phases: i) maintenance of a baseline voltage before stimulus application, ii) generation of a peak-like voltage at the onset of the stimulus, iii) decay to a specific value while the stimulus persists, and iv) generation of a peak-like voltage in the opposite direction upon stimulus removal. As previously discussed, the initial peak-like voltage is generated by the triboelectric mechanism, while the decay profile varies based on the electrical properties of the ionic component. By eliminating the influence of the dynamic

14

voltage—using the voltage measured 0.1 s after the dynamic voltage as a normalization reference—the correlation between the decay profile and the electrical properties of the ionic component can be identified. As shown in Fig. S6, consistent decay profiles are observed under identical thermal stimuli, highlighting the influence of variations in the electrical properties of the ionic component on temperature detection.

Based on the sensing mechanism of the p-TITS, the characteristic voltage profile can be described using a combination of two equations representing the triboelectric and ionic components (Fig. 4a). Before stimuli are applied (①), a stable state with a constant voltage value is maintained. When stimuli are applied (②), the triboelectric component generates charges, some of which are directly measured by the apparatus (③), whereas others interact with the ionic component (④), as shown in Fig. 4a.

Charges that directly flow to the measuring apparatus follow Eq. (1), which describes the voltage decay profile after charge generation, with amplitude A and decay constant B. Triboelectric charges are generated through contact electrification, in which electric charges are transferred between two different materials when they come into contact [57]. The amplitude A, which represents the amount of generated triboelectric charges, depends on several factors, including the triboelectric charge density, dielectric constant, surface area, material thickness, contact speed, and environmental conditions [58]. Except for the applied pressure and temperature, all other factors are considered to be constant, allowing the amplitude A to serve as an indicator of the triboelectric performance under stimuli. Since triboelectric charges are quickly dissipated through the measuring apparatus, which consists of resistors, a spike-like voltage profile with a very low decay constant B is observed [47]. The decay constant B, which is related to the resistance and capacitance of the system, was constant across all the cases, as the measurements were conducted under identical conditions.

Charges interacting with the ionic component follow Eq. (2), which is characterized by amplitude C and decay constant E. The behavior of charges interacting with ions resembles the discharge behavior of a capacitor, with the RC constant (E) serving as the decay constant [59]. Similarly, amplitude C represents the amount of charges interacting with ions, which is influenced by both the generated triboelectric charges and the electrical properties of the ionogel, as the effective charge varies with the applied stimuli. Unlike resistors, in which charges merely flow through them, capacitors allow charge accumulation, similar to the formation of an electric double layer at an electrode interface by ions. Since detection begins with the generation of triboelectric charges, some of which directly leak into the apparatus,

15

the interactions between ions and triboelectric charges involve a delay. Parameter D represents the delay time before charges start interacting with ions. A larger effective charge leads to a shorter delay time, corresponding to a lower D. The static voltage, denoted by F, is associated with the impedance of the p-TITS, as discussed regarding Fig. 3g-h. Eq. (1) describes charges flowing directly into the apparatus, unaffected by the ionogel, whereas Eq. (2) accounts for the decay behavior of charges interacting with ions. These two equations, derived from the theoretical understanding of the two distinct mechanisms, operate independently. Their summation, represented by Eq. (3), provides a comprehensive description of the overall voltage profile generated by the triboelectric charges.

$$y = A * exp\left(\frac{-x}{B}\right) \tag{1}$$

$$y = C * exp\left(\frac{-(x-D)}{E}\right) + F \tag{2}$$

$$y = A * exp\left(\frac{-x}{B}\right) + C * exp\left(\frac{-(x-D)}{E}\right) + F \tag{3}$$

By analyzing the amount and decay behavior of charges directly flowing through the measuring apparatus, parameters A and B can be determined. For the remaining charges that interact with ions, parameters C, D, E and F can be determined based on the charge amount and decay behavior. Under a stimulus of 5 N at 35 °C, parameters A, B, C, D, E and F were determined, as shown on the lower side of Fig. 4a, and Eq. (3) was fitted to the measured data, with an R^2 value of 0.973. The voltage profiles obtained under various stimulus conditions (temperature: 25 °C, 35 °C, 45 °C, pressure: 20 kPa, 50 kPa, 80 kPa) were fitted using Eq. (3) (Fig. S7). The correlation between the analytical and raw data across different stimuli yields an average R^2 value of 0.948, demonstrating a high degree of accuracy.

As depicted in Fig. S7, the parameter D, representing the delay time before charges start interacting with ions, tends to decrease with temperature regardless of pressure. Similarly, the parameter E, which serves as the decay constant of ions, tends to increase with temperature regardless of pressure. These trends indicate that an increase in the interfacial capacitance and a decrease in the impedance result in faster ion interactions with triboelectric charges and longer decay profiles, as previously shown in Fig. 3g, reflecting the dependence of the electrical properties of the p-TITS on the two types of stimuli. In addition, parameter B, which represents the RC constant of charges flowing into the measuring apparatus, is fixed.

16

Parameters A, C, and F, which are related to pressure stimuli, were also determined to achieve optimal fitting of the raw data (Fig. S8).

Fig. 4b presents the voltage profiles obtained under various pressure and temperature combinations. The data demonstrate a higher overall voltage with increasing pressure and an elongated decay profile with increasing temperature. To quantify these features, the dynamic voltage ($A+C+F$) and the RC constant (E) were utilized as key parameters. Since the RC constant (B) of the triboelectric component is fixed at 0.02, producing a peak-like voltage, determining the applied temperature using the RC constant (E) of the ionic component, which depends exclusively on thermal stimuli, is logical. Once the temperature is determined, the dynamic voltage can then be used to obtain the applied pressure, as the dynamic voltage increases with pressure under constant temperature conditions. As shown on the right side of Fig. 4b, the RC constant (E) of the ionic component, which represents the decay behavior of the ions influenced by the triboelectric charges, increases with temperature and remains constant at different pressures. This result demonstrates the temperature-sensing capability of the ionic component based on its RC constant. Under a defined temperature, the applied pressure can be effectively determined by measuring the dynamic voltage ($A+C+F$), as indicated by the bluish bar data. Therefore, the applied temperature and pressure can be effectively decoupled using the RC constant of the ionic component and the dynamic voltage.

As previously discussed, parameter A represents the triboelectric performance under stimulus application. The fitted A value increases with pressure and decreases with temperature, as shown by the gray points in Fig. 4c, which aligns with the experimental results in Fig. 3a-b. Considering the dominant factors affecting the electrical properties of the ionogel, a higher temperature increases the amount of effective charges, illustrated by an increased interfacial capacitance, as demonstrated in Fig. 3g. Correspondingly, the fitted C value also significantly increases with temperature compared with its variation with pressure, as indicated by the purple points in Fig. 4c.

By formulating the voltage profile using the given equation, the static pressure sensing mechanism can be further validated by analyzing parameter-derived values. To investigate the correlation between the impedance and the static pressure detection capability, as discussed regarding Fig. 3, the ratio of $C+F$ to F was calculated. This ratio represents the proportion of charges contributing to static voltage generation. The calculated ratio decreases with increasing temperature while showing minimal influence from pressure application (Fig. 4d). This trend reflects the corresponding variations in impedance with stimulus application.

17

The decreasing impedance of the ionic component with increasing temperature, irrespective of pressure application, as depicted in Fig. 3g, aligns with the ratio variations, supporting the origin of static voltage generation. By analyzing the voltage profile in terms of its triboelectric and ionic components, the sensing mechanism, which can be divided into two parts, is effectively validated.
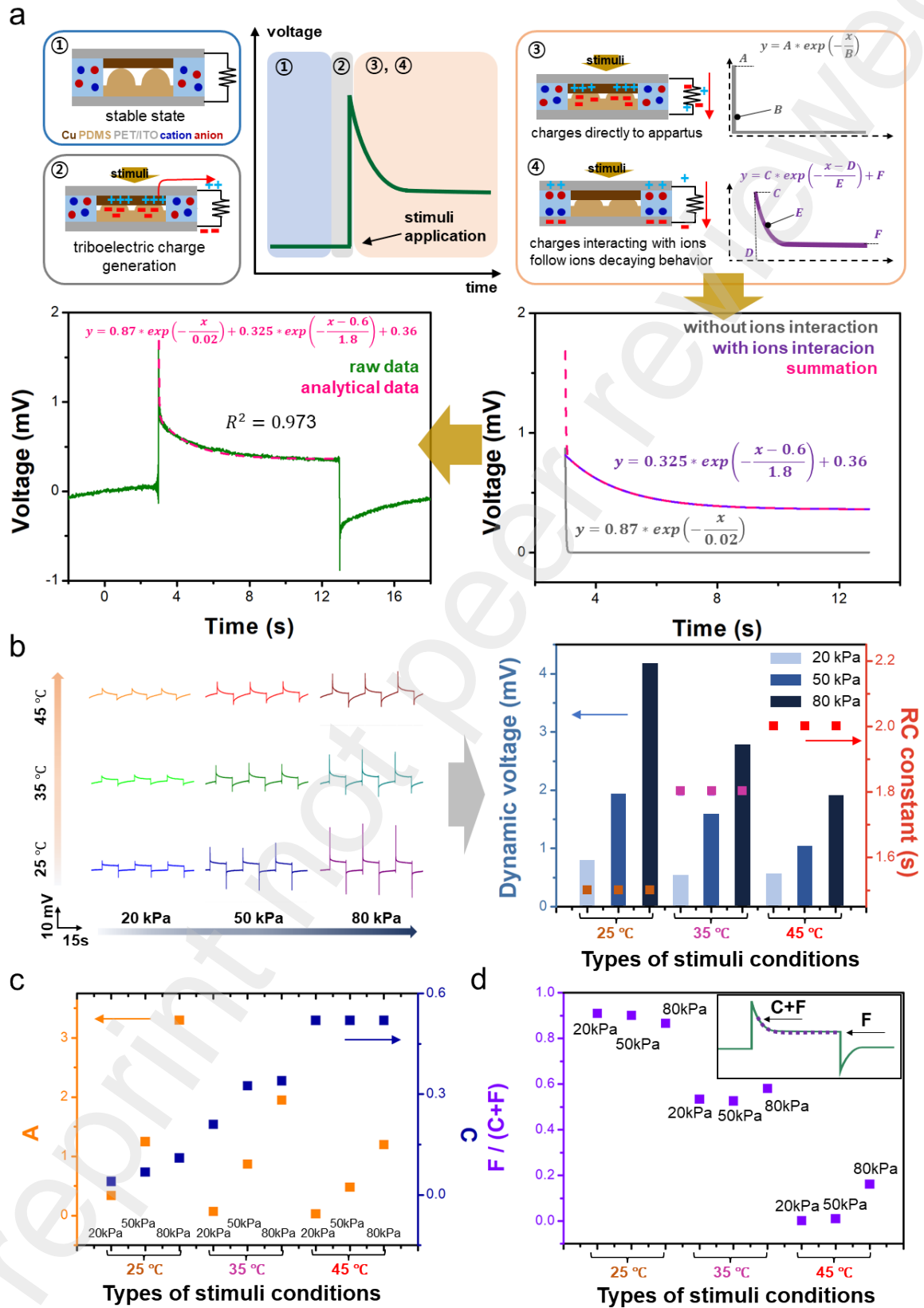
18

a

① stable state
Cu PDMS PET/ITO cation anion

② triboelectric charge generation

stimuli application

③ charges directly to appartus
$$y = A * exp\left(-\frac{x}{B}\right)$$

④ charges interacting with ions follow ions decaying behavior
$$y = C * exp\left(-\frac{x-D}{E}\right) + F$$

$$y = 0.87 * exp\left(-\frac{x}{0.02}\right) + 0.325 * exp\left(-\frac{x-0.6}{1.8}\right) + 0.36$$

raw data
analytical data

$$R^2 = 0.973$$

without ions interaction
with ions interacion
summation

$$y = 0.325 * exp\left(-\frac{x-0.6}{1.8}\right) + 0.36$$

$$y = 0.87 * exp\left(-\frac{x}{0.02}\right)$$

b

45 ℃   35 ℃   25 ℃

10 mV / 15s

20 kPa   50 kPa   80 kPa

20 kPa   50 kPa   80 kPa

Types of stimuli conditions

c

Types of stimuli conditions

d

C+F   F

Types of stimuli conditions

19

Figure 4. a) Behavior of triboelectric charges and ions upon stimulus application corresponding to the voltage profile, fitting of raw data by combining two equations of each component, namely, triboelectric and ionic, and its analysis. b) Voltage profiles, dynamic voltage, and RC constant under various pressures and temperatures. c-d) Analysis of parameters under various pressures and temperatures.

2.5. Application

Fig. 5a illustrates the real-time performance in discriminating pressure and temperature when using the p-TITS attached to a robotic claw. The p-TITS was mounted on one side of the robotic claw, which was operated via pulse width modulation (PWM). A constant voltage of 6 V and a PWM signal of 50 Hz at 5 V, with varying pulse width, were used to control the motion of the claw. As shown in Fig. S9a, two types of voltages were supplied to the robotic claw, and the p-TITS signal was wirelessly transmitted from an Arduino Nano to a Galaxy Tab S6 Lite (SM-P610) via a differential amplifier (MCP602). When the pulse width of the applied voltage was increased from 1.4 ms to 1.6 ms, the motor rotated, narrowing the robotic claw (Fig. S9b). By adjusting the claw displacement and altering the temperature of the object being grasped, pressure and temperature stimuli were simultaneously applied. Grabbing of a vial filled with water allowed the application of various pressures and temperatures by modifying the claw displacement and the water temperature.

The p-TITS was connected to pins 2 and 3 of the differential amplifier, which operated with a gain of 500. The output signal was transmitted to the Arduino Nano via pin 1 (Fig. S9c). The signal was subsequently smoothed for further analysis. The smoothed voltage signal, resembling the characteristic voltage profile in Fig. 1b, was monitored in real time (Movie S1). The voltage profile included a stable section followed by a rising section corresponding to the dynamic voltage peak. The voltage then decayed to a certain value, followed by a falling section. The average rate of change in the decaying voltage was calculated to estimate the temperature.

To evaluate the pressure-sensing capability, a greater pressure was applied by increasing the claw displacement. The peak values and values recorded between 0.01 s and 0.71 s were measured using Arduino. Higher pressures resulted in an overall upward shift in the voltage profile, as shown in Fig. S10a. To determine the temperature-detecting capability, the thermal stimulus was increased by increasing the temperature of the target material. As shown in Fig. S10b, values immediately after the peak (greenish region) and those used to calculate the

20

average rate of change during decay (reddish region for higher temperatures and bluish region for lower temperatures) were analyzed. Unlike Fig. S10a, in which the values in the greenish region differ due to pressure variations, Fig. S10b shows a relatively consistent range of the values in the greenish region when the same pressure is applied. However, higher thermal stimuli extend the decay profile, resulting in the reddish area being positioned higher than the bluish area, indicating a lower average rate of change.

These differences allowed the peak value to be used to determine pressure variations and the average rate of change to be used to determine temperature variations. The conversion of the average rates of change to temperature was based on the linear regression of the slope measured when vials containing water at 20 °C and 40 °C were gripped. The conversion of the peak values to pressure was derived from the relationship between the dynamic voltage and the applied stimuli (pressure, temperature), as discussed regarding Fig. 2e and 3b. The calculated pressure and temperature values were transmitted via a Bluetooth module (ZS-040), with the detailed procedure illustrated in Fig. S11. A smartphone app interface was developed by using App Inventor, and the corresponding block diagram is provided in Fig. S12. Real-time monitoring of applied stimuli through a wirelessly connected Galaxy Tab was demonstrated (Movie S2).

The softness of objects can be distinguished through the pressure-sensing capability by detecting both the dynamic pressure and static pressure [30]. Unlike approaches that require two separate pressure sensors to detect these two types of pressure, the p-TITS can detect both using a single sensor. Four target materials—glass, 10PDMS (10:1 weight ratio of the PDMS base and curing agent), 60PDMS (60:1 weight ratio of the PDMS base and curing agent), and a sponge—were selected for evaluation, and a pushing machine was used to assess the degree of softness of the target materials, revealing a gradient of increasing softness from glass to the sponge (Fig. 5b). An initial load of 0.5 N was applied to ensure contact with the target materials, followed by an additional 4 N. The displacements of the four materials under the additional load were measured (Fig. S13). The soft sponge exhibits the largest displacement (1.3 mm) under the 4 N load, whereas the harder glass shows minimal displacement (0.25 mm), indicating that softer materials exhibit greater displacement under the same pressure.

Similarly, when the p-TITS presses the four types of target materials, softer materials induce larger displacements. Since the p-TITS contains an air gap inside, which is softer than the target materials, most of the displacement occurs within the sensor itself. Larger

21

displacements between the upper and lower parts of the p-TITS result in greater deformation of the structured PDMS, generating more triboelectric charges when softer materials are pressed, as depicted on the left side of Fig. 5c.

The classification of the material softness was further verified using machine learning. A load of 4 N was applied following the initial 0.5 N, and the four target materials (glass, 10PDMS, 60PDMS, sponge) were pressed 72 times each using the pushing machine, resulting in 288 datasets. The datasets were randomly split, with 20% (60 datasets) used for testing and the remaining 80% (228 datasets) used for training the machine learning model. Each dataset contained time and voltage data representing the voltage profile under pressure application. The training datasets were classified into the four types of materials, and the RandomForestClassifier model was used for training. The model achieves an accuracy of 98.33%, with the confusion matrix displayed on the right side of Fig. 5c. The detailed procedure, implemented using Google Colab, is provided in Fig. S14.

Fig. 5d illustrates the softness perception capability by demonstrating the robotic claw grasping various objects: an apple as a hard object, a plum tomato and a shine muscat as medium-hardness objects, and a sponge as a soft object. All the objects were cut to the same size of 2.6 cm to ensure consistency, and the robotic claw operated based on displacement, narrowing over a duration of 5 s. Since harder objects undergo less compression under the same displacement, they induce higher dynamic voltages. This trend contrasts with the results shown in Fig. 5c, where softer objects induce higher dynamic voltages. This discrepancy arises from the different methodologies used: in the previous step, the same pressure was applied using a pushing machine, whereas in the current setup, pressure was applied based on uniform displacement variations. Additionally, the time elapses before the appearance of the dynamic voltage increases for softer objects.

As the hardness increases, the ratio between the static voltage and the dynamic voltage decreases [30]. Among the tested materials, the hard apple has the lowest ratio, whereas the sponge has the highest ratio (Fig. 5d). The two fruits with similar softness, the plum tomato and shine muscat, display comparable dynamic voltages and similar static-to-dynamic voltage ratios, confirming the effectiveness of this metric as an indicator of softness. By detecting both dynamic and static pressures, the reliability of softness perception is significantly enhanced, enabling a more comprehensive assessment of material properties.

Fig. 5e provides a detailed analysis of the interactions with soft targets susceptible to damage. To enable the p-TITS to handle objects in real-life scenarios, delicate control is

22

essential when manipulating soft materials such as fruits. A sponge representing a non-damageable target and a banana representing a damageable target were selected for evaluation. After initial contact, additional pressure was applied to simulate squeezing, which could lead to damage. When the robotic claw maintains its displacement during the initial touch, both materials exhibit voltage signal increment followed by decay profiles. Upon application of an additional pressure at approximately 5 s, the materials are further compressed to simulate a squeezing motion. The sponge demonstrates additional voltage increment and decay profiles, yet it remains undamaged throughout the squeezing process. In contrast, the banana displays a decreased peak voltage, resembling the behavior when the claw detaches from the material.

When the target material retains its elasticity and remains undamaged, the load between the material and the p-TITS remains balanced, enabling the applied force to be evenly distributed between the material and the sensor. However, when this balance is disrupted due to material damage, the target loses its structural integrity and cannot resist the force of the sensor. At the moment of damage, the load applied to the p-TITS decreases, resulting in a sudden drop in the voltage profile, similar to a load release. This phenomenon is clearly depicted on the right side of Fig. 5e, where the damage point in the voltage profile of the damaged banana is highlighted, marked by a red circle.

In addition to assessing the softness of target materials, the p-TITS can also regulate the holding force for soft materials. By detecting and responding to the moment of material failure, damage can be prevented, ensuring safe and precise manipulation of delicate objects.

3. Conclusion

We developed a self-powered sensor capable of simultaneously detecting dynamic pressure, static pressure, and temperature. The detection process begins with the generation of a triboelectric signal, followed by its decay, which is governed by the interactions between ions and the generated charges. The triboelectric pressure sensor facilitates the detection of dynamic pressure while supplying the charges necessary for additional stimuli detection. The variations in the impedance and interfacial capacitance of the ionogel enable the generation of static pressure signals and ensure distinct signal profiles under various temperatures.

Importantly, an analytical formula for the characteristic voltage profiles can be derived by combining two equations, each representing one of the sensing components: triboelectric and ionic. The parameters within the exponential decay equations exhibit tendencies

23

corresponding to the triboelectric and electrical properties of each component, validating the simultaneous sensing mechanism for the three types of stimuli. Furthermore, the varying voltage profile, which encodes information about the applied thermal stimulus and pressure, can be quantified through parameters that effectively discriminate between the stimuli.

Pressure and temperature stimuli can be distinguished by first determining the temperature, followed by the pressure, as triboelectric signals are influenced by temperature. By quantifying the elongated profile through the average rate of change, the applied temperature and pressure can be detected in real time. Additionally, the ability to sense both dynamic and static pressures allows the sensor to evaluate the softness of grasped objects by calculating the ratio between the dynamic and static voltages. Object impairments can also be identified through a drop in the peak voltage, resembling detachment from the stimulus.

The ability to detect three stimuli, representing the fundamental tactile senses of skin, using a single sensor highlights the potential of the p-TITS for high-resolution sensing. The analytical formula with parameters grounded in physical principles provides deeper insight into interactions with various objects, capturing not only their features but also the dynamics of interacting motions. Moreover, the self-powered design minimizes the need for additional components, such as signal processors or batteries, thereby simplifying systems used in applications such as smart prosthetics, robotics, and extended reality (XR) technologies.
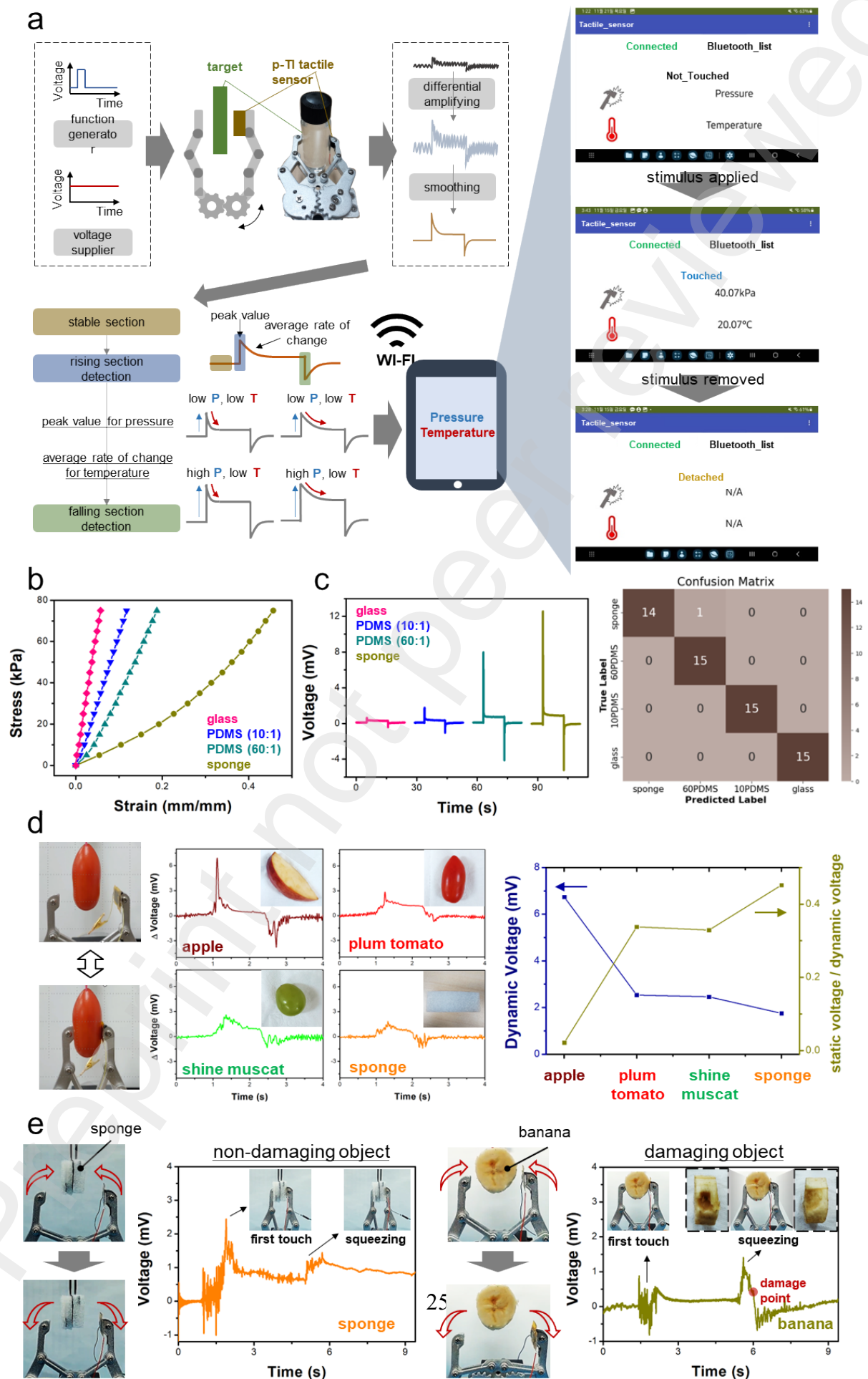
24

Figure 5. a) Wireless real-time performance in discriminating pressure and temperature, along with the detailed procedure. b) Compression test of sensing targets with various softness values. c) Voltage profiles and classification test confusion matrix for softness recognition derived from the p-TITS. d) Softness identification of objects grasped by a robotic claw. e) Detection of the damage moment during squeezing of non-damageable and damageable objects.

4. Experimental Section/Methods

4.1. Materials

PU (Hydromed D4) was purchased from Advan Source Biomaterials. [EMIM][BF$_4$], PET/ITO electrodes, (3-aminopropyl)triethoxysilane (APTES), and trichloro(1H,1H,2H,2H-perfluorooctyl)silane were obtained from Sigma Aldrich, USA. Photocurable resin (high-temperature resin) was purchased from Formlabs, USA. Ethanol was acquired from Duksan General Science, South Korea, and deionized water was sourced from Sungwoo Genetehc Co., Ltd., South Korea. Al foil (16 μm thickness) was purchased from Samjin Aluminum, South Korea. PDMS (Sylgard 184 elastomer kit) was obtained from Dow Corning. Carbon tape was purchased from TERAOKA SEISAKUSHO Co., Ltd., Japan.

4.2. Fabrication of the triboelectric component

Sixteen negative hemispherical patterns with a diameter of 1 μm were designed using AutoCAD (Fig. S1b). The patterns were 3D printed (Form 3, Formlabs), and the fabricated template was UV cured at 80 °C for 3 h and annealed at 150 °C for an additional 3 h. Pt was deposited on the surface of the template to prevent the liquid PDMS from reacting with the uncured resin in the template. A self-assembled monolayer (SAM) of trichloro(1H,1H,2H,2H-perfluorooctyl)silane was vacuum-deposited onto the template for 30 min and annealed at 120 °C for 1 h. PDMS (with a 10:1 ratio of the base to the curing agent) was spin-coated onto the treated template at 800 rpm for 10 s. The thickness of the structured PDMS was measured to be approximately 270 μm. The PDMS-coated template was vacuum treated to allow uncured PDMS to permeate the negative pattern of the template without forming air gaps and then annealed at 120 °C until fully cured. fThe template with cured PDMS was oxygen plasma treated (CUTE, Femto Science), and a 1 wt% APTES aqueous solution was applied on the surface of the cured PDMS. The surface-treated PDMS was cut into 1 cm × 1 cm pieces and detached from the template to complete fabrication of the

26

structured PDMS. Aluminum foil was used as the counter triboelectric contact layer for the structured PDMS.

4.3. Fabrication of the ionic component

A PU solution (10 wt% dissolved in an EtOH and DI water solution with a weight ratio of 19:1) was prepared by stirring at 50 °C. After the solution was ready, 4 wt% [EMIM][BF$_4$] ionic liquid was added to the PU solution and magnetically stirred until a uniform, transparent solution was obtained. The PU/[EMIM][BF$_4$] solution was then dropped onto a trichloro(1H,1H,2H,2H-perfluorooctyl)silane SAM-coated Si-wafer substrate and dried in a humidity-controlled chamber of 25% humidity for 3 d to fabricate a 300 μm-thick PU ionogel. The concentration of the ionic liquid was optimized based on the stability of the ionogel. A high concentration of the ionic liquid compared to the PU polymer led to instability caused by a drying issue (Fig. S2b,c).

4.4. Integration of the triboelectric component and ionic component

The detailed fabrication procedure is illustrated in Fig. S1c. A 1 cm × 2 cm piece of carbon tape was attached to a 1 cm × 2.5 cm PET/ITO electrode, and the fabricated structured PDMS was conformally attached to the center of the carbon tape. The PU ionogel was cut into a 0.5 cm × 1 cm piece and attached to the remaining sides of the carbon tape. A 1 cm × 1 cm piece of Al foil was attached to another 1 cm × 2.5 cm PET/ITO electrode using carbon tape, and a PU/[EMIM][BF$_4$] solution was drop cast onto the remaining part of the PET/ITO electrode to facilitate attachment of the PU ionogel. After the drop-cast PU/[EMIM][BF$_4$] was dried to form a PU ionogel, both PET/ITO electrodes were assembled so that the structured PDMS directly contacted the Al foil, whereas the PU ionogels contacted each other beside the triboelectric component.

4.5. Measurements

Material characterization was performed using a field emission scanning electron microscope (JEOL-FE-SEM, IT-500HR), a thermogravimetric analyzer (TA Instruments, SDT Q600), and a surface profiler (DektakXT Stylus Profile, Bruker). Electrochemical measurements were carried out using a potentiostat (SP-300, Biologic), a digital multimeter (DMM 6500, Tektronix), and an LCR meter (E4980AL, Keysight). Pressure was uniformly applied to the sensor using a custom-built pushing machine (Limotion Systems). Temperature was uniformly applied to the sensor via a DC voltage supply (UP36-6, TDK-Lambda). The movement of the robotic claw (6DOF metallic robot arm, Scipia) was controlled by an

27

arbitrary function generator (AFG1062, Tektronix) and a DC voltage supply (UP36-6, TDK-Lambda).

Data Availability Statement

Data will be made available on request.

Acknowledgments

Appendix A. Supporting information

References

[1] A. Chortos, J. Liu, Z. Bao, Pursuing prosthetic electronic skin, Nat. Mater. 15 (2016) 937-950. https://doi.org/10.1038/nmat4671

[2] V.E.Abraira, D.D.Ginty, The sensory neurons of touch, Neuron. 79 (2013) 618−639. http://dx.doi.org/10.1016/j.neuron.2013.07.051

[3] A.E.Dubin, A.Patapoutian, Nocicpetors: the sensors of the pain pathway, J Clin Invest. 120(11) (2010) 3760-3772. https://doi.org/10.1172/JCI42843

[4] S.Chun, J.S.Kim, Y.Yoo, Y.Choi, S.J.Jung, D.Jang, G.Lee, K.I.Song, K.S.Nam, I.Youn, D.Son, C.Pang, Y.Jeong, H.Jung, Y.J.Kim, B.D.Choi, J.Kim, S.P.Kim, W.Park, S.Park, An artificial neural tactile sensing system, Nat.Electron. 4 (2021) 429-438. https://doi.org/10.1038/s41928-021-00585-x

[5] J.Lee, S.Kim, S.Park, J.Lee, W.Hwang, S.W.Cho, K.Lee, T.Y.Seong, C.Park, S.Lee, H.Yi, 2022. An artificial tactile neuron enabling spiking representation of stiffness and disease diagnosis. Adv.Mater. 2201608. https://doi.org/10.1002/adma.202201608

[6] P.Zhu, Z.Li, J.Pang, P.He, S.Zhang, 2024. Latest developments and trends in electronic skin devices. Soft Sci. 4:17. https://dx.doi.org/10.20517/ss.2024.05

[7] P.Li, H.P.A.Ali, W.Cheng, J.Yang, B.C.K.Tee, 2020. Bioinspired prosthetic interfaces. Adv.Mater.Technol. 5, 1900856. https://doi.org/10.1002/admt.201900856

[8] L.E.Osborn, A.Dragomir, J.L.Betthauser, C.L.Hunt, H.H.Nguyen, R.R.Kaliki, N.V.Thakor, 2018. Prosthesis with neuromorphic multilayered e-dermis perceives touch and pain. Sci.Robot. 3, eaat3818. http://doi.org/10.1126/scirobotics.aat3818

28

[9]   Y.H.Jung, B.Park, J.U.Kim, T.Kim, 2019. Bioinspired electronics for artificial sensory systems. Adv.Mater. 31, 1803637. http://doi.org/10.1002/adma.201803637

[10]   Z.H.Guo, H.L.Wang, J.Shao, Y.Shao, L.Jia, L.Li, X.Pu, Z.L.Wang, 2022. Bioinspired soft electroreceptors for artificial precontact somatosensation. Sci.Adv. 8(21), eabo5201. https://doi.org/10.1126/sciadv.abo5201

[11]   W.Li, K.Ke, J.Jia, J.Pu, X.Zhao, R.Bao, Z.Liu, L.Bai, K.Zhang, M.Yang, W.Yang, 2022. Recent advances in multiresponsive flexible sensors toward E-skin: a delicate design for versatile sensing. Small. 18, 2103734. https://doi.org/10.1002/smll.202103734

[12]   J.Chen, Y.Zhu, X.Chang, D.Pan, G.Song, Z.Guo, N.Naik, 2021. Recent progress in essential functions of soft electronic skin. Adv.Funct.Mater. 31, 2014686. https://doi.org/10.1002/adfm.202104686

[13]   D.Filingeri, Humidity sensation, cockroaches, worms and humans: are common sensory mechanisms for hygrosensation shared across species? J Neurophysiol. 114 (2015) 763-767. https://doi.org/10.1152/jn.00730.2014

[14]   Z.Yuan, G.Shen, Materials and device architecture towards a multimodal electronic skin, Mater.Today. 64 (2023) 165-179. https://doi.org/10.1016/j.mattod.2023.02.023

[15]   R.Yang, W.Zhang, N.Tiwari, H.Yan, T.Li, H.Cheng, 2022. Multimodal sensors with decoupled sensing mechanisms. Adv.Sci. 9, 2202470. https://doi.org/10.1002/advs.202202470

[16]   C.Zhu, D.Guo, D.Ye, S.Jiang, Y.Huang, Flexible PZT-integrated, bilateral sensors via transfer-free laser lift-off for multimodal measurements. ACS Appl.Mater.Interfaces. 12 (2020) 37354-37362. https://dx.doi.org/10.1021/acsami.0c10083

[17]   P.Zhu, Y.Wang, Y.Wang, H.Mao, Q.Zhang, Y.Deng, 2020. Flexible 3d architecture piezo/thermoelectric bimodal tactile sensor array for e-skin application. Adv.Energy Mater. 10, 2001945. https://doi.org/10.1002/aenm.202001945

[18]   S.Sharma, G.B.Pradhan, S.Jeong, S.Zhang, H.Song, J.Y.Park, Stretchable and all-directional strain-insensitive electronic glove for robotic skins and human-machine interfacing. ACS Nano. 17 (2023) 8355-8366. https://doi.org/10.1021/acsnano.2c12784

[19]   S.Pyo, J.Lee, K.Bae, S.Sim, J.Kim, 2021. Recent progress in flexible tactile sensors for human-interactive systems: from sensors to advanced applications. Adv.Mater. 33, 2005902. https://doi.org/10.1002/adma.202005902

29

[20] J.Wu, X.Fan, X.Liu, X.Ji, X.Shi, W.Wu, Z.Yue, J.Liang, Highly sensitive temperature-pressure bimodal aerogel with stimulus discriminability for human physiological monitoring. Nano Lett. 22 (2022) 4459-4467. https://doi.org/10.1021/acs.nanolett.2c01145

[21] X.Fu, Z.Zhuang, Y.Zhao, B.Liu, Y.Liao, Z.Yu ,P.Yang, K.Liu, Stretchable and self-powered temperature-pressure dual sensing ionic skins based on thermogalvanic hydrogels. ACS Appl.Mater.Interfaces. 14 (2022) 44792-44798. https://doi.org/10.1021/acsami.2c11124

[22] Y.Wang, H.Wu, L.Xu, H.Zhang, Y.Yang, Z.L.Wang, 2020. Hierarchically patterned self-powered sensors for multifunctional tactile sensing. Sci.Adv. 6:eabb9083. https://doi.org/10.1126/sciadv.abb9083

[23] F.Zhang, Y.Zang, D.Huang, C.Di, D.Zhu, 2015. Flexible and self-powered temperature-pressure dual-parameter sensors using microstructure-frame-supported organic thermoelectric materials. Nat.Commun. 6:8356. https://doi.org/10.1038/ncomms9356

[24] S.Han, F.Jiao, Z.U.Khan, J.Edberg, S.Fabiano, X.Crispin, 2017. Thermoelectric polymer aerogels for pressure-temperature sensing applications. Adv.Funct.Mater. 27, 1703549. https://doi.org/10.1002/adfm.201703549

[25] X.Ma, C.Wang, R.Wei, J.He, J.Li, X.Liu, F.Huang, S.Ge, J.Tao, Z.Yuan, P.Chen, D.Peng, C.Pan, Bimodal tactile sensor without signal fusion for user-interactive applications. ACS Nano. 16 (2022) 2789-2797. https://doi.org/10.1021/acsnano.1c09779

[26] K.Song, R.Zhao, Z.L.Wang, Y.Yang, 2019. Conjuncted pyro-piezoelectric effect for self-powered simultaneous temperature and pressure sensing. Adv.Mater. 31, 1902831. https://doi.org/10.1002/adma.201902831

[27] M.Ma, Z.Zhang, Z.Zhao, Q.Liao, Z.Kang, F.Gao, X.Zhao, Y.Zhang, 2019. Self-powered flexible antibacterial tactile sensor based on triboelectric-piezoelectric-pyroelectric multi-effect coupling mechanism. Nano Energy. 66, 104105. https://doi.org/10.1016/j.nanoen.2019.104105

[28] Y.E.Shin, Y.J.Park, S.K.Ghosh, Y.Lee, J.Park, H.Ko, 2022. Ultrasensitive multimodal tactile sensors with skin-inspired microstructures through localized ferroelectric polarization. Adv.Sci. 9, 2105423. https://doi.org/10.1002/advs.202105423

30

[29] S.Chun, W.Son, H.Kim, S.K.Lim, C.Pang, C.Choi, Self-powered pressure- and vibration-sensitive tactile sensors for learning technique-based neural finger skin. Nano Lett. 19 (2019) 3305-3312. https://doi.org/10.1021/acs.nanolett.9b00922

[30] J.W.Fastier-Wooller, T.Vu, H.Nguyen, M.Rybachuk, Y.Zhu, D.V.Dao, V.T.Dau, Multimodal fibrous static and dynamic tactile sensor. ACS Appl.Mater.Interfaces. 14 (2022) 27317-27327. https://doi.org/10.1021/acsami.2c08195

[31] X.Fu, J.Dong, L.Li, L.Zhang, J.Zhang, L.Yu, Q.Lin, J.Zhang, C.Jiang, J.Zhang, Y.Wang, W.Wu, F.Fan, Y.Wang, Q.Yang, 2022. Fingerprint-inspired dual-mode pressure sensor for robotic static and dynamic perception. Nano Energy. 103, 107788. https://doi.org/10.1016/j.nanoen.2022.107788

[32] J.Park, M.Kim, Y.Lee, H.S.Lee, H.Ko, 2015. Fingertip skin-inspired microstructured ferroelectric skins discriminate static/dynamic pressure and temperature stimuli. Sci.Adv. 1:e1500661. https://doi.org/10.1126/sciadv.1500661

[33] S.Bi, X.Zhao, F.Gao, X.Xun, B.Zhao, L.Xu, T.Ouyang, Q.Liao, Y.Zhang,. A high-sensitive and self-selective humanoid mechanoreceptor for spatiotemporal tactile stimuli cognition. Nano Res. 17 (2023) 4400-4409. https://doi.org/10.1007/s12274-023-6248-z

[34] S.Kim, W.Cho, J.Hwang, J.Kim, 2023. Self-powered pressure sensor for detecting static and dynamic stimuli through electrochemical reactions. Nano Energy. 107, 108109. https://doi.org/10.1016/j.nanoen.2022.108109

[35] P.Delmas, J.Hao, L.Rodat-Despoix, Molecular mechanisms of mechanotransduction in mammalian sensory neurons. Nat.Rev.Neurosci. 12 (2011) 139-153. https://doi.org/10.1038/nrn2993

[36] J.C.Yang, J.Mun, S.Y.Kwon, S.Park, Z.Bao, S.Park, 2019. Electronic skin: recent progress and figures prospects for skin-attachable devices for health monitoring, robotics, and prosthetics. Adv.Mater. 31, 1904765. https://doi.org/10.1002/adma.201904765

[37] H.Cao, S.Cai, 2022. Recent advances in electronics skins: material progress and applications. Front Bioeng Biotechnol. 10:1083579. https://doi.org/10.3389/fbioe.2022.1083579

[38] K.Xu, Y.Lu, K.Takei, 2019. Multifunctional skin-inspired flexible sensor systems for wearable electronics. Adv.Mater.Technol. 4, 1800628. https://doi.org/10.1002/admt.201800628

31

[39] J.Kang, J.B.-H.Tok, Z.Bao, Self-healing soft electronics. Nat.Electron. 2 (2019) 144-150. https://doi.org/10.1038/s41928-019-0235-0

[40] Y.Peng, N.Yang, Q.Xu, Y.Dai, Z.Wang, 2021. Recent advances in flexible tactile sensors for intelligent systems. Sensors. 21, 5392. https://doi.org/10.3390/s21165392

[41] U.P.Claver, G.Zhao, 2021. Recent progress in flexible pressure sensors based electronic skin. Adv.Eng.Mater. 23, 2001187. https://doi.org/10.1002/adem.202001187

[42] Q.Li, L.Zhang, X.Tao, X.Ding, 2017. Review of flexible temperature sensing networks for wearable physiological monitoring. Adv.Healthcare.Mater. 6, 1601371. https://doi.org/10.1002/adhm.201601371

[43] B.A.Kuzubasoglu, S.K.Bahadir, 2020. Flexible temperature sensors: a review. Sens.Actuators.A.Phys. 315, 112282. https://doi.org/10.1016/j.sna.2020.112282

[44] S.Korkmaz, I.A.Kariper, 2021. Pyroelectric nanogenerators (PyNGs) in converting thermal energy into electrical energy: fundamentals and current status. Nano Energy. 84, 105888. https://doi.org/10.1016/j.nanoen.2021.105888

[45] J.Qin, L.Yin, Y.Hao, S.Zhong, D.Zhang, K.Bi, Y.Zhang, Y.Zhao, Z.Dang, 2021. Flexible and stretchable capacitive sensors with different microsturctures. Adv.Mater. 33, 2008267. https://doi.org/10.1002/adma.202008267

[46] C.Zhao, Y.Wang, G.Tang, J.Ru, Z.Zhu, B.Li, C.F.Guo, L.Li, D.Zhu, 2022. Ionic Flexible sensors: mechanisms, materials, structures, and applications. Adv.Funct.Mater. 32, 2110417. https://doi.org/10.1002/adfm.202110417

[47] J.H.Lee, Y.S.Park, S.Cho, I.S.Kang, J.K.Kim, U.Jeong, Output voltage modulation in triboelectric nanogenerator by printed ion gel capacitors. Nano Energy. 54 (2018) 367-374. https://doi.org/10.1016/j.nanoen.2018.10.016

[48] E.Lee, J.Park, 2022. A self-powered, single-mode tactile sensor based on sensory adaptation using piezoelectric-driven ion migration. Adv.Mater.Technol. 7, 2200691. https://doi.org/10.1002/admt.202200691

[49] Y.Xiong, J.Han, Y.Wang, Z.L.Wang, Q.Sun, 2022. Emerging iontronic sensing: materials, mechanisms, and applications. Research. 2022. https://doi.org/10.34133/2022/9867378

[50] Y.Chang, L.Wang, R.Li, Z.Zhang, Q.Wang, J.Yang, C.F.Guo, T.Pan, 2021. First decade of interfacial iontronic sensing: from droplet sensors to artificial skins. Adv.Mater. 33, 2003464. https://doi.org/10.1002/adma.202003464

[51]   S.Wang, X.Fan, Z.Zhang, Z.Su, Y.Ding, H.Yang, X.Zhang, J.Wang, J.Zhang, P.Hu, A skin-inspired high-performance tactile sensor for accurate recognition of object softness. ACS Nano. 18 (2024) 17175-17184.
https://doi.org/10.1021/acsnano.4c04100

[52]   H.Chen, I.Furfaro, E.F.Lavado, S.P.Lacour, 2024. Liquid metal-based sensor skin enabling haptic perception. Adv.Funct.Mater. 34, 2308698.
https://doi.org/10.1002/adfm.202308698

[53]   S.Lee, J.Park, 2022. Fingerprint-inspired triboelectric nanogenerator with a geometrically asymmetric electrode design for a self-powered dynamic pressure sensor. Nano Energy. 101, 107546. https://doi.org/10.1016/j.nanoen.2022.107546

[54]   S.Sharma, P.Chand, 2023. Supercapacitor and electrochemical techniques: a brief review. Results Chem. 5, 100885. https://doi.org/10.1016/j.rechem.2023.100885

[55]   C.X.Lu, C.B.Han, G.Q.Gu, J.Chen, Z.W.Yang, T.Jiang, C.He, Z.L.Wang, 2017. Temperature effect on performance of triboelectric nanogenerator. Adv.Eng.Mater. 19, 1700275. https://doi.org/10.1002/adem.201700275

[56]   X.Wu, J.Zhu, J.W.Evans, C.Lu, A.C.Arias, 2021. A potentiometric electronic skin for thermosensation and mechanosensation. Adv.Funct.Mater. 31, 2010824.
https://doi.org/10.1002/adfm.202010824

[57]   W.Kim, D.Kim, I.Tcho, J.Kim, M.Kim, Y.Choi, Triboelectric nanogenerator: structure, mechanism, and applications. ACS Nano. 15 (2021) 258-287.
https://dx.doi.org/10.1021/acsnano.0c09803

[58]   R.D.I.G.Dharmasena, S.R.P.Silva, Towards optimized triboelectric nanogenerators. Nano Energy. 62 (2019) 530-549. https://doi.org/10.1016/j.nanoen.2019.05.057

[59]   D.Halliday, R.Resnick, J.Walker, Fundamentals of Physics, Wiley, Hoboken, NJ, USA 2001.

33